



# Blue Laser Conduction Spot Welding of Pure Copper Hairpins

Spot welding of copper hairpins by a blue laser was conducted, resulting in better weld quality and efficiency than with a conventional infrared laser

BY Z. J. TANG, L. WAN, X. L. ZHANG, C. L. ZHU, H. H. YANG, Y. B. HAO, K. ZHAO,  
M. CHIUMENTI, Y. WU, H. W. WANG, AND H. Z. WANG

## Abstract

Joining rectangular copper hairpins significantly improves the performance of hairpin motors. Copper welding poses a significant challenge due to its low laser absorptivity when using conventional infrared lasers. Although employing keyhole welding with a high-power and small-spot infrared laser can increase the absorption rate through multi-reflections, it introduces instabilities caused by the multi-recoil forces within the keyhole and the absorptivity differences among solid, liquid, and keyhole states of copper. The proposed solution adopts a 450 nm blue laser, which exhibits a superior laser absorptivity toward copper and facilitates stable conduction mode spot welding with an enlarged laser spot. This research achieved successful blue laser conduction spot welding of copper hairpins with a gap and, for the first time, systematically analyzed the force and instability factors of a molten pool. The results demonstrated that with a laser power of 1950 W, laser spot diameter of 0.6 mm, and defocusing amount of -3 mm, only 0.7 s of welding time was required to join copper hairpins with a 0.6 mm gap. Notably, there were no noticeable defects in weld beads during blue laser welding. Meanwhile, the study identified recoil force as a significant uncertain factor inducing defects, particularly in the keyhole mode. Compared to infrared technology, the blue laser, characterized by a higher absorption rate and a larger spot diameter, effectively reduced uncertainty through conduction welding. This research showcased the significant potential for blue lasers in manufacturing copper hairpin motors.

## Keywords

- Hairpin Motor
- Laser Welding
- Blue Laser
- Copper
- Molten Pool

## Introduction

The hairpin motor is an electric motor that uses a hairpin-shaped winding to generate torque. It is characterized by high torque and efficiency and low noise and vibration, making it suitable for high-power applications. With the rapid development of new electric vehicles, the automotive industry is looking for enhanced requirements to produce hairpin motors with higher power and torque, smaller size, and higher rotation speed, among other improved performance factors. The rectangular copper wire connection in the hairpin motor has an essential effect on the final performance.

The leading technologies for joining rectangular copper wires are electron beam welding and conventional infrared laser welding. Tóth et al. (Ref. 1) tried to join copper wires with electron beam welding by reciprocating scanning. Though the electron beam can overcome the low absorption of copper, its cost is high. Dimatteo et al. (Ref. 2) and Glaessel et al. (Ref. 3) applied infrared laser scanner welding to join copper wires with almost no gap. The weld beads showed some pores, and the process parameter window was small. Blom et al. (Ref. 4) presented that copper's infrared laser absorption rates with different states were quite different. The absorption rate for solid copper was very low: about 3%. For liquid copper, the rate was about 15%. After forming a keyhole, the rate suddenly increased to about 60%. The large variation of absorption rate in different states makes it difficult to regulate energy input. Meanwhile, when increasing the absorption rate through the keyhole, the multi-reflections in the keyhole may also lead to an unstable molten pool and unreliable qualities.

Compared to the conventional infrared laser, the blue laser has a much higher absorption for copper, up to 65% (Refs. 5, 6). The blue laser has been applied in additive manufacturing, welding, etc. For additive manufacturing, Tang et al. (Ref. 7) proved that the blue laser allowed for the directed energy deposition (DED) of aluminum alloys using a lower power supply and achieved better performance than with an infrared laser. For welding, Tang et al. (Ref. 8) presented that when a gap existed between laminated sheets, a large-spot flat-top blue laser had an advantage in restabilizing the molten pool. Tang et al. (Ref. 9) also applied a blue laser for the bead-on-plate welding of copper and aluminum. The results showed that a 2000 W blue laser could weld conventional high-reflectivity metals (e.g., copper and aluminum) in conduction mode and without spatters. Fujio et al. (Ref. 10) tried spot welding a single pure copper wire by combining a blue-infrared hybrid laser. The spot diameters of the blue laser and infrared laser were 0.055 mm and 0.2 mm. There were no apparent spatters during the welding process. Zediker et al. (Ref. 11) joined two rectangular copper wires adopting a 500 W blue laser, showing promising results. Thus, the blue laser is a keyhole-free technology with an improved absorption rate when welding high-reflectivity materials. Blue laser welding does not rely on the keyhole produced by high energy density focused in very small spot size for the infrared laser. Larger spot size can stabilize the molten pool, thus avoiding defects, such as pores. Meanwhile, the larger spot size allows spot welding, which is more efficient with simpler welding processes and optical structures.

Zediker et al. confirmed the feasibility of blue laser spot welding of pure copper hairpins (Ref. 11). However, the welding ability has not been systematically demonstrated as being of fundamental importance. Very high process quality must guarantee stable molten pool dynamics, as Sun et al. (Ref. 12) showed by in-situ monitoring and adaptive control. Moreover, there will be a gap between the hairpins for a surplus when assembling, unavoidable assembly errors, and enriching the structural design. The gap may affect the stability of the molten pool. Tang et al. (Ref. 8) found a self-stabilization of the molten pool due to surface tension when a gap was found in conduction welding. Guo et al. (Ref. 13) studied the influence of gaps on the stability of molten pool flow and pore defect generation in keyhole welding. They could show that a 16  $\mu\text{m}$  gap was enough to block welding continuity. Therefore, when the blue laser welding copper hairpins have a gap, the dynamic behavior of the molten pool also needs to be clarified.

This work applied 2000 W blue laser spot welding to rectangular copper wires. First, the molten pool's dynamic behavior was shown. Based on this, the welding strategy was optimized. Next, the metallographic, micro-hardness, and electrical resistance were analyzed. Finally, blue and infrared laser welding technologies were compared.

## Experimental Setup and Methods

### Experimental Setup

The experimental setups are shown in Fig. 1. The blue laser welding system included a blue laser generator (LDMblue 2000-60 VG7H, Laserline GmbH, Mülheim-Kärlich, Germany), a welding head (Laserline OTS-5 blue optics-welding),

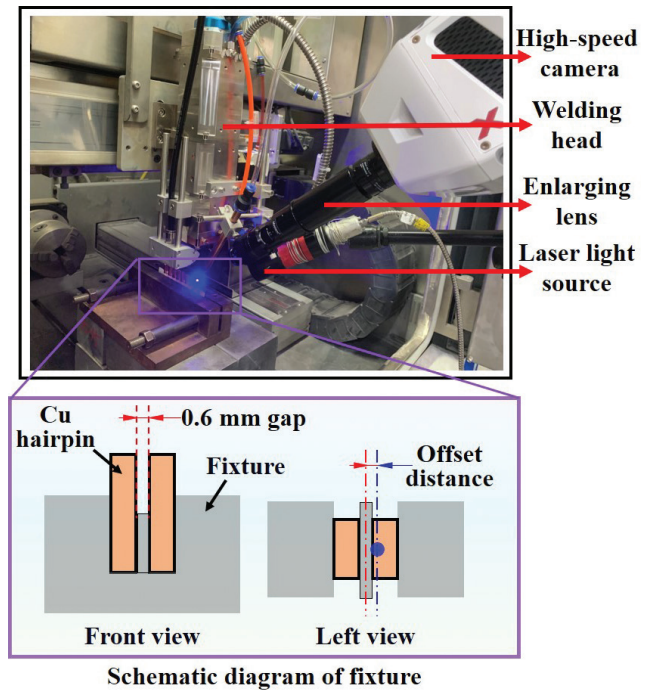


Fig. 1 — Experimental setups of the blue laser welding system with the fixture and the molten pool monitoring device.

a 3-axis displacement platform (X/Y/Z 400/300/400 mm, Raycham Co. Ltd., Nanjing, China), and a cooling-water machine (MCWL-15ODTR, Tongfei Co. Ltd., Sanhe, China). The energy distribution of the blue laser beam was flat-top. A fiber with a diameter of 0.6 mm was applied to transfer energy from the blue laser generator to the welding head. The focal lengths of the collimating and focusing lenses were 112 mm when the laser wavelength was 450 nm. The beam quality was 60 mm mrad. When the laser defocused on the surface of the specimen, the spot diameter was about 0.6 mm. Argon as the shielding gas was delivered to the weld area with a constant value of 900 L/h. A fixture was applied to fix the samples with a constant gap of 0.6 mm. A high-speed camera (Revealer X213, AgileDevice Co. Ltd., Hefei, China) with 3000 FPS and 1.3 Mpix was utilized to obtain the dynamic behavior. The viewing angle of the high-speed camera was about 45 deg. The distance from the lens to the observed molten pool was about 30 mm. Meanwhile, this work applied a laser light source and optical filter with 808 nm wavelength to avoid the interference of complex spectrums from the molten pool. The camera started collecting 1 s earlier than the laser and stopped collecting data 1 s after the laser ended, ensuring the whole dynamic behavior was captured.

### Materials and Welding Procedure

This work chose commercial copper (T1), the main material of copper winding wires in the hairpin motor, as the experimental material. Its chemical composition is listed in Table 1. The specimen dimension was 4 mm  $\times$  2 mm  $\times$  40 mm. All specimens were polished to avoid the interference of oxide scale and greasy dirt. Two specimens were fixed with a 0.6

**Table 1 – Chemical Composition of Copper (T1)**

Chemical Element	Copper	Other
Mass Fraction (wt-%)	> 99.95	< 0.05

**Table 2 – Process Parameter Design of Blue Laser Spot Welding of Copper Hairpins**

Process Parameter	Value
Laser Power (W)	1950
Welding Time (s)	0.3, 0.5, 0.7, 0.9, and 1.1
Defocusing Amount (mm)	+3, 0, -3, -5, and -7
Offset Distance (mm)	0, 0.3, 0.4, 0.5, and 0.6

mm gap by a fixture, as shown in Fig. 1. The laser irradiated the upper surface of the specimen vertically. The specimens and the laser welding head both remained fixed during welding. The experiment considered four process parameters: laser power, spot welding time, defocusing amount, and offset distance. The selected process parameters are listed in Table 2.

The laser power was set to 1950 W, the maximum power value for the highest processing efficiency, when designing the process parameters. The welding time was the time of blue laser radiation. The defocusing amount was the distance between the specimen's upper surface and the laser's focal point. The focal point was determined by first adjusting the laser spot to the visual minimum; the height coordinate of the laser head was  $z$ . Then, the laser was turned on to weld a spot every 0.1 mm in the  $z - 0.5$  to  $z + 0.5$  mm interval. The laser process time of each spot was 0.2 s. The  $z$  value for the smallest and most apparent spot was the position where the defocus amount was 0 mm. The offset distance was the distance between the center of the blue laser beam and the centerline of the two copper hairpins, as shown in Fig. 1. Based on many preliminary experiments, the welding times were 0.3, 0.5, 0.7, 0.9, and 1.1 s. The defocusing amounts were +3, 0, -3, -5, and -7 mm. The offset distances were chosen as 0, 0.3, 0.4, and 0.5 mm. The three parameters were investigated according to the determination process of each process parameter in the actual processing. First, different offset distances were tried to ensure the horizontal position of the welding head. Second, various defocusing amounts were researched to determine the height of the welding head. Last, welding times were adjusted to optimize efficiency.

## Characterization Methods

The samples were cut by an electron discharge machining in the middle of the welded joint perpendicular to the 4 mm long side. An automatic polishing machine (Saphir 530, ATM

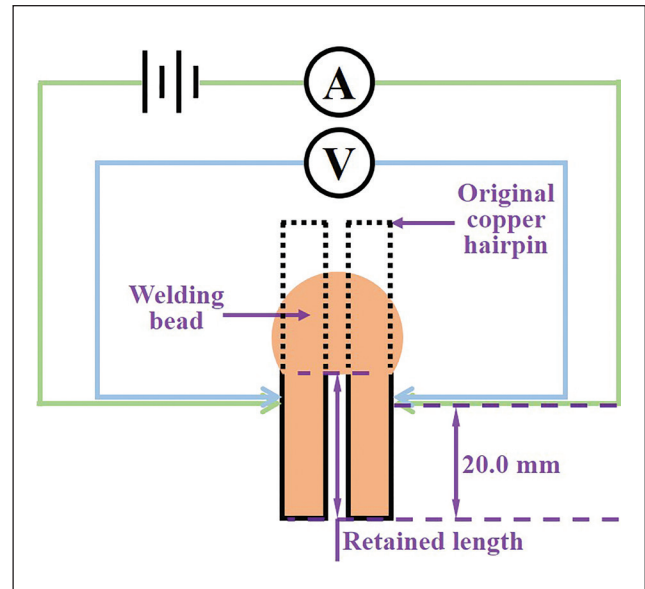


Fig. 2 – Sketch for measuring resistance and retained length.

Qness GmbH, Mammelzen, Germany) was applied to ensure uniform sample removal. The cross section of the welded joint was ground by 80 to 2500-grade and was polished using 5, 1.5, and 0.5  $\mu\text{m}$  diamond suspension solutions. Finally, metallographic corrosion was performed with a ferric chloride (5 g), hydrochloric acid (25 ml), and ethanol (100 ml) solution. The etching time was about 20 s. The metallographic structure was analyzed by a laser scanning confocal microscope (VK-X3000, Keyence Co. Ltd., Shanghai, China). Metallographic data were collected for three cross sections of each sample and averaged. Each new cross section was directly reground and repolished without redundant removal.

The measuring positions are shown in Fig. 2. Resistance value is a critical electrical property in copper hairpin welding. The Kelvin four-terminal sensing method was used for resistance measurement. The measurement sketch for the resistance and retained length is shown in Fig. 2. All data were measured three times and averaged.

## Results

### Molten Pool Characteristics

According to the order of spot welding, the laser spot position was the first process parameter. The offset distance,  $d$ , was set as 0, 0.3, 0.4, 0.5, and 0.6 mm, as seen in Table 2. The results showed that offset distance is critical to the success or failure of welding. There were three main welding effects under different offset distances. When the offset distance was 0.6 mm, there was usually only one hairpin that could be melted, as shown in Fig. 3A. With an offset distance of 0 mm, almost all the laser beam energy radiated into the gap. Little metal could be melted, as exhibited in Fig. 3B. The molten pool characteristics when the offset distance was 0.3, 0.4, or 0.5 mm are shown in Fig. 4. The

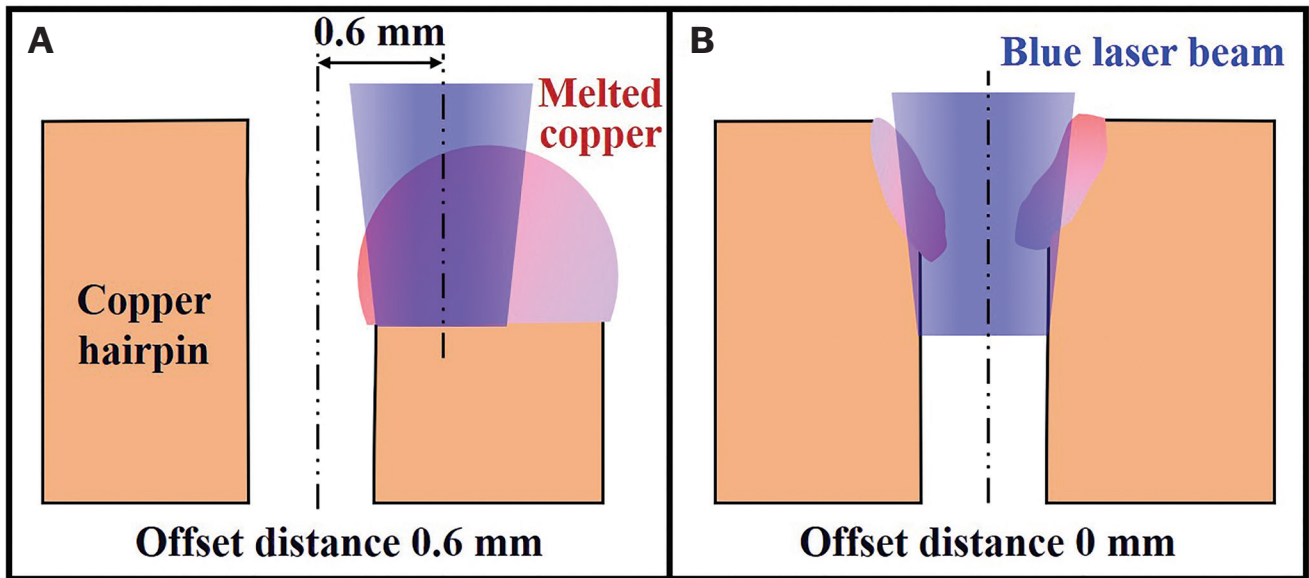


Fig. 3 – Sketch of typical inapposite laser spot position, offset distance, and welding effects: A – 0.6 mm offset distance; B – 0 mm offset distance.

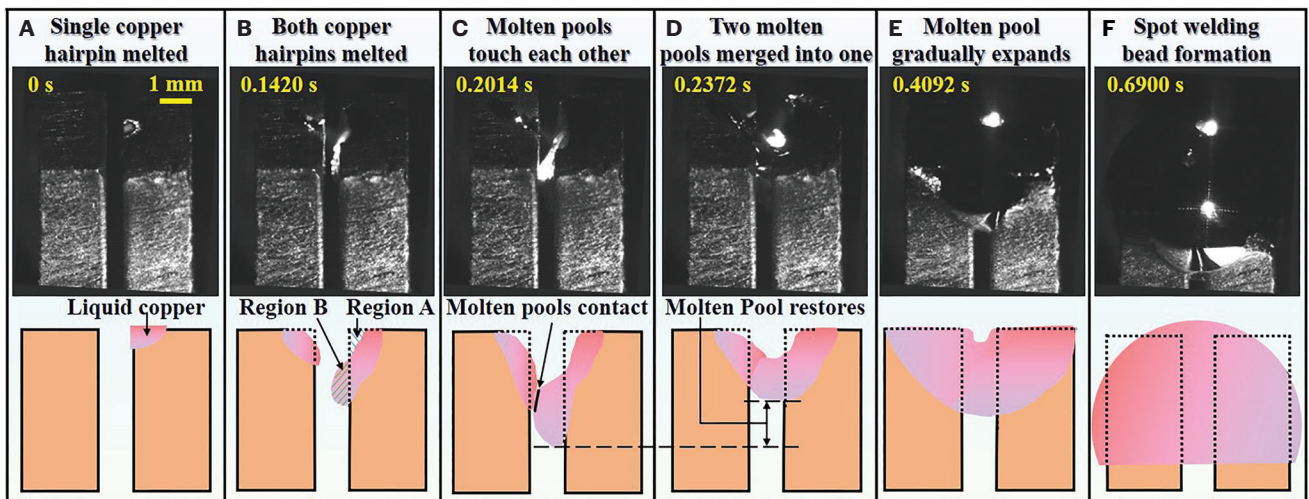


Fig. 4 – Molten pool dynamic behavior with 1950 W laser power, 0.7 s welding time, -5 mm defocusing amount, and 0.5 mm laser offset distance (the data acquisition rate was 5000 fps).

difference between different offset distances was mainly in the success rate of welding and the melting speed of the copper hairpin. After five experiments for each offset distance, the 0.5 mm offset distance initially received the most laser energy while ensuring a more-efficient success rate. At last, the 0.5 mm offset distance was chosen in the following research about the welding time and defocusing amount.

Figure 4 shows the welding process. First, a single copper hairpin began to melt, as seen in Fig. 4A. Second, two copper hairpins melted together, as seen in Fig. 4B. Third, the two molten pools of liquid copper merged into the same one (Figs. 4C and D). Finally, the molten pool gradually expanded and formed a weld bead, as shown in Figs. 4E and F. The dynamic behavior of the molten pool had an obvious signifi-

cance on welding qualities and efficiencies, which will be discussed in the section “Dynamic Behavior of the Molten Pool.” The “Process Parameters Optimization Strategy” section will show how to optimize the process further according to dynamic behavior.

### Weld Bead Appearance

According to the design sequence of process parameters, the offset distance determines the horizontal position of the welding head. The defocusing amount determines the vertical position of the welding head. The welding time determines the final laser processing time.

The weld bead appearances with different defocusing amounts and welding times at the constant offset distance

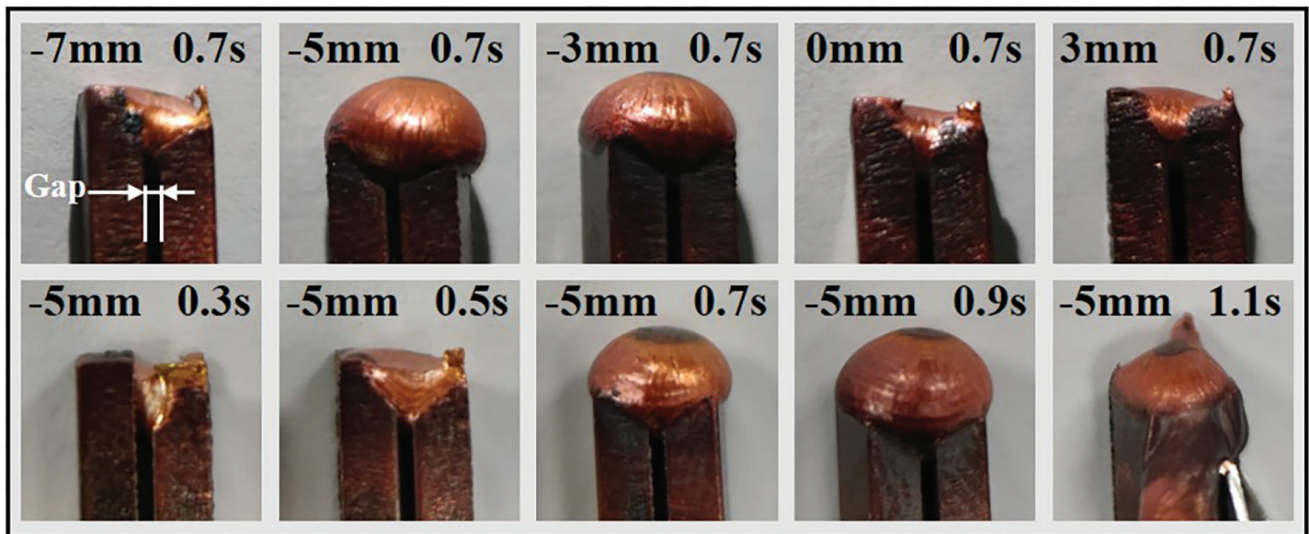


Fig. 5 – Weld bead appearances with different defocusing amounts and welding times when the gap was 0.6 mm.

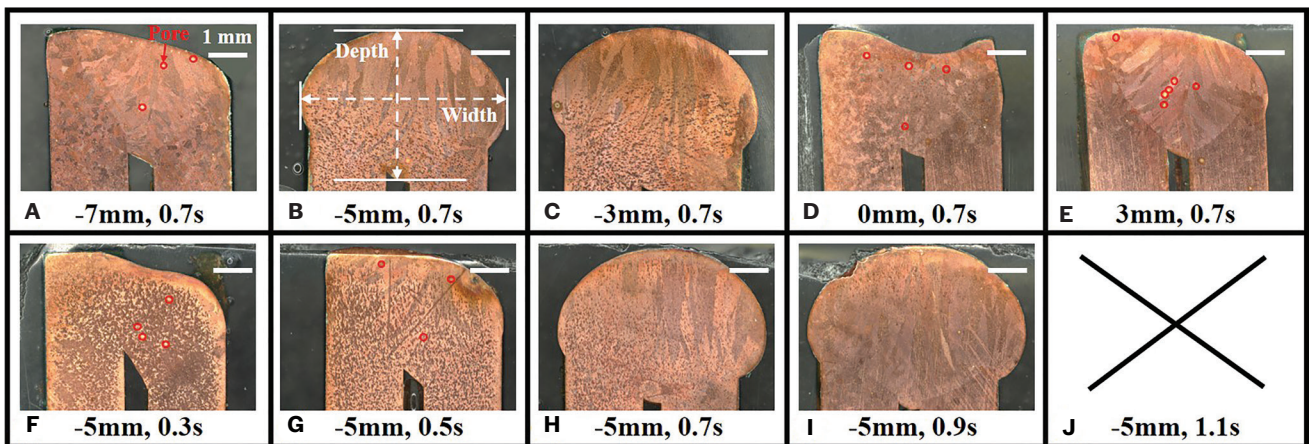


Fig. 6 – Cross section pictures with different process parameters. The numbers on the left are the defocusing amounts and those on the right are the welding times.

of 0.5 mm are shown in Fig. 5. The results showed that the ideal near-spherical weld bead could not be formed with too large or too small defocusing amounts. Among them, the weld bead appearance at the defocusing amount of -5 mm was relatively ideal. A fixed -5 mm defocus amount and different welding times can clearly show the changing trend of the weld beads' appearance and the retained molten pool characteristics. At 0.3 s, the hairpins on both sides melted, forming a molten pool to create a weld bead. At 0.5 s, the weld bead area expanded to cover the surface of the copper hairpins. The melted copper at 0.7 s increased and formed a near-spherical weld bead due to surface tension. At 0.9 s, weld bead size increased. At 1.1 s, the near-spherical molten pool slipped off and the welding process failed.

### Cross Section Image and Dimension

Figure 6 shows the cross section images with different process parameters. When the welding time was short, or the defocusing amount was unsuitable for the cross section, the height difference between the two copper hairpins was noticeable, as shown in Figs. 6A, D, and F. The welding process ended when the two molten pools merged into one, as seen in Fig. 4. With an increase in the welding time or more concentrated energy, the heights of the two hairpins gradually leveled out, as shown in Figs. 6E and G. At that moment, the molten pool gradually expanded but did not yet form a near-spherical weld bead. When a more-complete weld bead was created, the weld beads were near-spherical.

Pores are a key aspect of weld quality. In Fig. 6, the gray-scale of the pore is large because the pore region was not in the focal plane and reflected the light. Compared with the defocusing amount of -3 mm, a defocusing amount of -5 mm can lead to fewer pores. When the welding time increased,

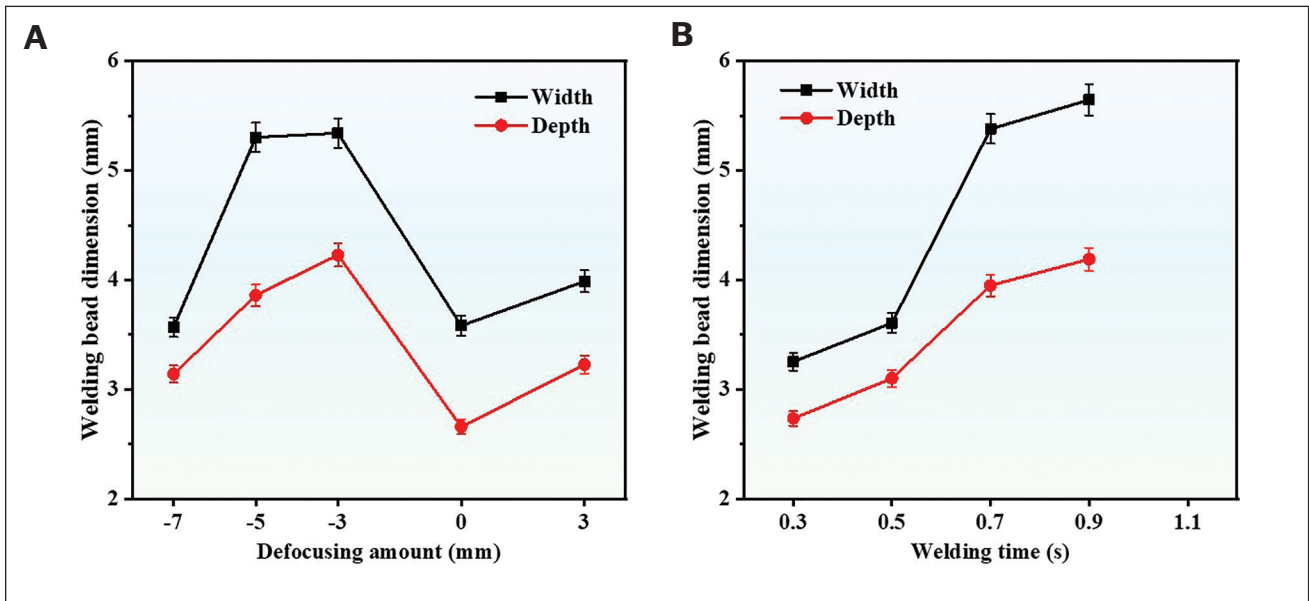


Fig. 7 – A – Influence of defocusing amount with a constant welding time of 0.7 s; B – influence of welding time with the constant defocusing amount of -5 mm on the width and depth of welding beads.

the solid copper melted more fully, and there were fewer pores because of the violent flow.

The influence of process parameters on spot weld bead dimensions is shown in Fig. 7. The results showed that the variation trends of weld bead widths and depths were consistent. The defocusing amount and the welding time directly impacted bead dimensions. Corresponding to Fig. 5, the width and depth dimensions were larger when the appearance was ideal.

## Electrical Resistance

Electrical resistance is an important indicator for hairpins. The defocusing amount and welding time influenced resistance, as shown in Figs. 8A and B. The result showed that when the welding time increased, the spot welding process gradually completed with a lower resistance, except for the welding time of 1.1 s. When the welding time was too long, such as 1.1 s, the molten pool was unstable, leading to a failure weld. When the defocusing amount increased, resistance decreased then increased and, at last, decreased; the variation tendency was the same as that of the weld bead size. The retained hairpin lengths with different process parameters are shown in Figs. 8C and D. The results were consistent with the variation tendency of resistance. The welding time had a more obvious influence on resistance; when the defocusing amount was -3 or -5 mm, electrical performance and appearance were better.

## Discussions

### Dynamic Behavior of the Molten Pool

The dynamic behavior of the molten pool is shown in Fig. 4. First, a single copper hairpin irradiated by the laser began to melt. Then, due to high temperature and laser energy reflection,

two copper hairpins melted together. When enough metal material was melted on both hairpins, contact occurred, and the liquid copper in the two hairpins merged into the same molten pool. At last, as the welding time went on, the molten pool gradually expanded and formed a weld bead. Bai et al. (Ref. 14) presented that dynamic behaviors were important for process optimization, mechanism explanation, and in-situ control. The processes in Fig. 4 can be divided into three stages to understand the dynamic behavior better and facilitate systematic analysis.

1. First stage. The two regions were not in contact at this stage, as shown in Figs. 4A and B. Considering the defocusing location and offset distance, the copper hairpins melted simultaneously or sequentially. With continuous energy input, the metal in Region A moved to Region B, as shown in Fig. 4B. Region B in the gap decided when the welding process could transfer to the second stage.

2. Second stage. The second stage began with two adjacent molten pools touching and finished when the molten pool was stable, as seen in Figs. 4C and D. The key point of this stage was when the molten pool in the gap backfilled and recovered smoothly. To clarify the process, the equilibrium of forces of the liquid copper in the gap is exhibited in Fig. 9. In this process, four forces acting on the liquid copper in the gap formed a control body in the equilibrium of forces. These forces included the shielding gas impact force  $F_s$ , recoil force  $F_e$ , gravity force  $G$ , and restore force  $F_r$ . Figure 9C shows a local force analysis. During spot welding, the fixed position will be continuously impacted by a large flow rate of shielding gas. The shielding gas impact force  $F_s$  of the local region is calculated as follows:

$$F_s = Q^2 \rho_{Ar} / S_{Ar}^2 \quad (1)$$

where  $Q$  is the flow rate of shielding gas,  $\rho_{Ar}$  is the Ar density, and  $S_{Ar}$  is the cross-section area of the shielding gas feed pipe.

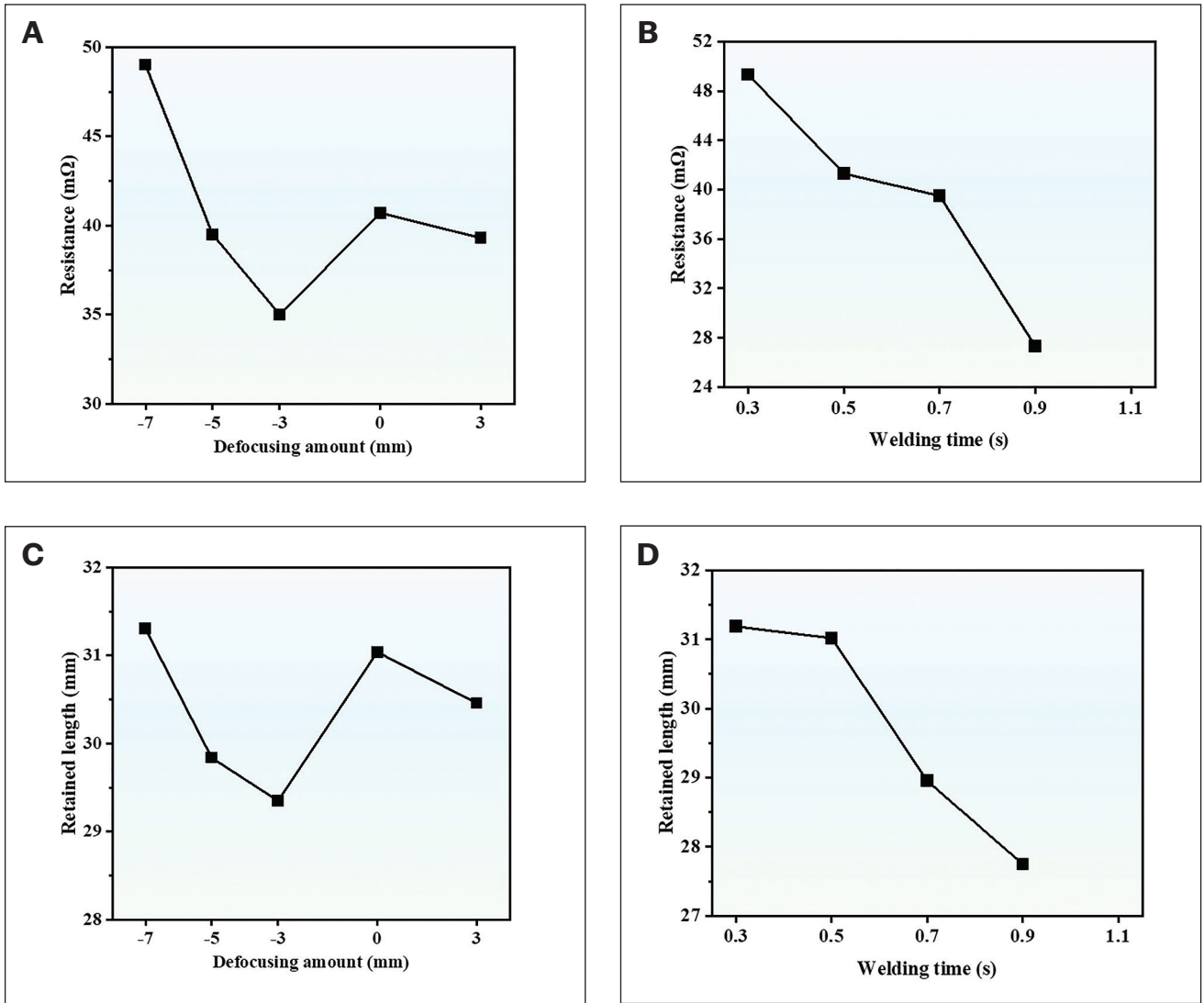


Fig. 8 – A – Influence of defocusing amount on resistance with a constant welding time of 0.7 s; B – influence of welding time on resistance with a constant defocusing amount of -3 mm; C – influence of defocusing amount on retained length with a constant welding time of 0.7 s; D – influence of welding time on retained length with a constant defocusing amount of -3 mm.

The recoil force  $F_e$  of the local region generates from the depression and potential metallic vapor (Ref. 15), which is written as:

$$F_e = S_L(P_e - P_0) \quad (2)$$

with the surface pressure of the molten pool  $P_e$  written as:

$$P_e = \begin{cases} P_{amb} \\ 0.5(1 + \beta_R)P_0 \exp\left(\frac{mL_v(1 - \frac{T_v}{T_s})}{k_B T_v}\right) \\ 0 \leq T_s < T_v \\ + \infty > T_s \geq T_v \end{cases} \quad (3)$$

where  $P_{amb}$  is the ambient pressure,  $\beta_R$  is the coefficient that represents the fraction of recondensation particles to evaporations ones,  $S_L$  is the local region area,  $P_0$  is the atmospheric pressure,  $m$  is the mass per atom,  $L_v$  is the latent heat of vaporization,  $T_v$  is the boiling temperature under  $P_0$ ,  $T_s$  is the molten pool temperature of the local region, and  $k_B$  is the Boltzmann constant. Because the influence of dramatic fluctuation of the keyhole after the change of welding mode is difficult to quantify, the equation mainly considers the impact of the recoil force generated by heating and evaporation.

Gravity,  $G$ , relates the liquid metal in the gap, with the following formula:

$$G = V_{cu}' \rho_{cu} g, \quad (4)$$

where  $V_{cu}'$  is the liquid metal volume of the local region,  $\rho_{cu}$  is the density of copper, and  $g$  is the gravitational acceleration.

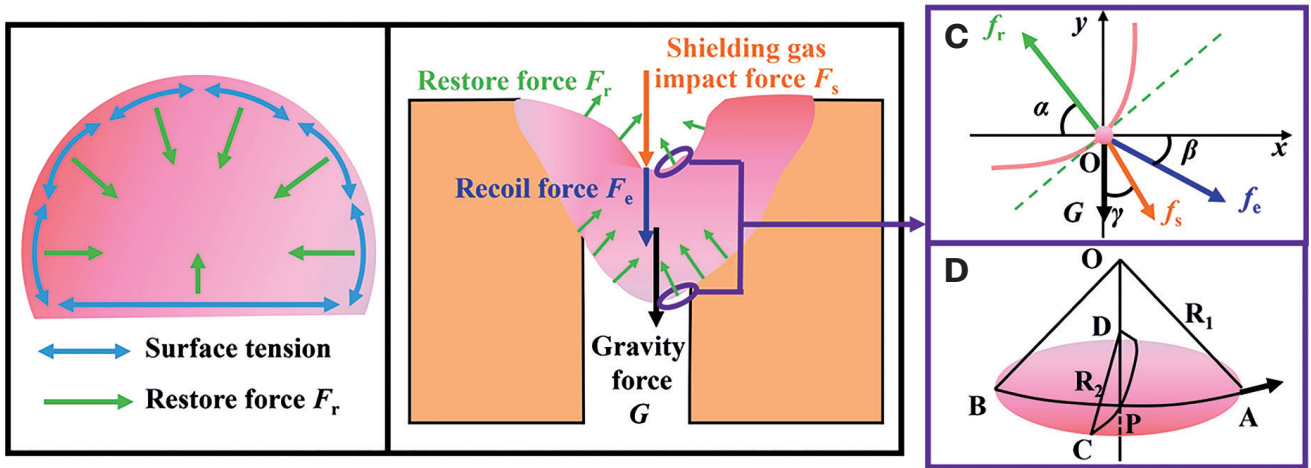


Fig. 9 – Force analysis of the molten pool when two molten pools touch each other: A – The relationship between the surface tension and restoring force; B – the global force analysis; C – the local force analysis; D – surface tension calculation parameters.

Surface tension leads to the restoring force  $F_r$  of the local region. The restoring force makes the liquid metal contract inward. When the molten pool outline changes, the surface tension analysis can be seen in Figs. 9A and D. Based on the Young-Laplace equation, the restoring force  $F_r$  reads:

$$F_r = \gamma(1/R_1 + 1/R_2)S_L, \quad (5)$$

where  $\gamma$  is the surface tension coefficient which depends on the temperature of the local region.  $R_1$  and  $R_2$  are the radii of the curvature circle.

Due to the equilibrium of forces in the local description of liquid copper, the local forces can be given explicitly:

$$\begin{cases} \sin \alpha \cdot F_r = \cos \sigma \cdot F_s + \sin \beta \cdot F_e + G \\ \cos \alpha \cdot F_r = \sin \sigma \cdot F_s + \cos \beta \cdot F_e \end{cases} \quad (6)$$

The transformation of equilibrium of forces from local description to global description can be given by integration of local force vectors on the surfaces  $S_1$  and  $S_2$ :

$$\begin{cases} F_r = \int_{S_1} \vec{F}_r d\vec{S} + \int_{S_2} \vec{F}_r d\vec{S} \\ F_e = \int_{S_1} \vec{F}_e d\vec{S} \\ F_s = \int_{S_1} \vec{F}_s d\vec{S} \\ G = \rho V g \end{cases} \quad (7)$$

where  $S_1$  is the upper surface and  $S_2$  is the lower surface. To facilitate the theoretical calculation, Fig. 9B shows a simplified schematic diagram of force analysis, which assumes that the internal temperature of the molten pool is uniform and the surface tension coefficient is set to 1.25 N/m in the following calculations (Ref. 16). Considering Equation 7,  $F_s$ ,  $F_e$ ,  $G$ , and  $F_r$  can be written as follows:

$$F_s = S_F Q^2 \rho_{Ar} / S_{Ar}^2, \quad (8)$$

$$F_e = \begin{cases} S_F \cdot (P_{amb} - P_0) \\ S_F \cdot \left( 0.5(1 + \beta_R) P_0 \exp\left(\frac{mL_v(1 - \frac{T_v}{T_s})}{k_B T_v}\right) - P_0 \right) \end{cases} \quad (9)$$

$$\begin{cases} 0 \leq T < T_{vb} \\ +\infty > T \geq T_{vb}' \end{cases}$$

$$G = V_{Cu} \rho_{Cu} g, \quad (10)$$

$$F_r = \gamma[(1/R_{11} + 1/R_{12})S_{r1} + (1/R_{21} + 1/R_{22})S_{r2}] \quad (11)$$

where  $S_F$  is the depression area;  $V_{Cu}$  is the liquid metal volume in the gap;  $R_{11}$ ,  $R_{12}$ , and  $S_{r1}$  are the relative parameters of the upper surface tension;  $R_{21}$ ,  $R_{22}$ , and  $S_{r2}$  are the relative parameters of the lower surface tension. To solve Equations 8–11, the geometric parameters of the molten pool in the gap can be estimated and simplified, as shown in Fig. 10. Therefore, the geometric parameters can be rewritten as follows:

$$\begin{cases} S_F \approx W_F W_{mol} \\ V_{Cu} \approx W_{gap} R_2 W_{mol} \\ S_{r1} \approx S_F \\ S_{r2} \approx \pi W_{mol}^2 / 4 \\ R_{11} \approx R_{12} \approx R_1 \\ R_{21} \approx R_{22} \approx R_2 \end{cases} \quad (12)$$

**Table 3 — Cummulation Parameters and Results of the Force Status**

Parameter	Value	Data Source
Q (L/h)	900	Experimental setup
$\rho_{Ar}$ (kg/m <sup>3</sup> )	1.65	—
$S_{Ar}$ (mm <sup>2</sup> )	12.60	Actual Measurement
$W_{gap}$ (mm)	0.60	Experimental Setup
$S_f$ (mm <sup>2</sup> )	1.10	Eq. 7
$W_f$ (mm)	0.52	Fig. 4
$B_R$	0~1	Ref. 17
$P_o$ (Mpa)	0.1	—
$M$ (g)	$1.06 \times 10^{-22}$	Ref. 18
$L_v$ (kJ/mol)	300.3	Ref. 19
$T_v$ (°C)	2560	Ref. 20
$T_s$ (°C)	1083~3000	Ref. 20
$K_B$ (J/K)	$1.380649 \times 10^{-23}$	—
$V_{Cu}$ (mm <sup>3</sup> )	1.89~5.04	Eq. 7
$W_{mol}$ (mm)	2.1	Fig. 4
$\rho_{Cu}$ (kg/m <sup>3</sup> )	$8.9 \times 10^3$	Ref. 21
$g$ (m/s <sup>2</sup> )	9.8	—
$\gamma$ (N/m)	1.25	Ref. 16
$R_1$ (mm)	0.3~1.5	Fig. 4
$R_2$ (mm)	1.5~4.0	Fig. 4
$S_{r1}$ (mm <sup>2</sup> )	1.10	Eq. 7
$S_{r2}$ (mm <sup>2</sup> )	3.46	Eq. 7
$F_s$ (N)	$7.15 \times 10^{-4}$	Eq. 8
$F_e$ (N)	0~0.32 ( $\beta_R = 0$ ) 0~0.76 ( $\beta_R = 1$ )	Eq. 9
$G$ (N)	$(1.65 \sim 4.40) \times 10^{-4}$	Eq. 10
$F_r$ (N)	$(0.40 \sim 1.50) \times 10^{-2}$	Eq. 11

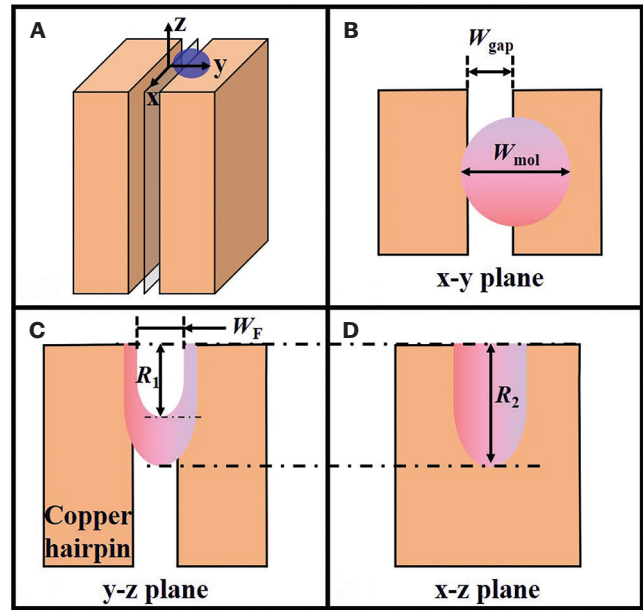


*Fig. 10 — Schematic diagram of molten pool parameters used for the force calculation: A — 3D coordinates; B — molten pool x-y plane; C — molten pool y-z plane; D — molten pool x-z plane.*

After preliminary cumulation, the results are listed in Table 3. In past research, Tang et al. (Ref. 8) analyzed the force of the molten pool when meeting a gap. The result showed that surface tension force, as the restoring force  $F_r$ , was much larger than the gravity force  $G$ . For the gravity force  $G$ , the result in Table 3 is similar to the result in Reference 8. However, for the shielding gas impact force  $F_s$ , when the shielding gas rate changed from 900 to 1800 L/h, the  $F_s$  increased to  $2.9 \times 10^{-3}$  N, which was close to the restoring force  $F_r$ . If pursuing the shielding effect, the high flow of argon may degrade welding qualities. In addition, it can be found that the recoil force  $F_e$  will change significantly with some parameters. With a change in molten pool temperature,  $F_e$  can change from 0 to 0.32 or 0.76 N, which will be much larger than  $F_r$ , as shown in Fig. 11. It means some violent behaviors of the molten pool (for example, the keyhole welding resulting from the high energy density) have the possibility to against the molten pool restoring and then produce defects. Therefore, the conduction mode has advantages when spot welding with a gap.

3. Third stage. At this stage, the molten pool stably melted the copper hairpins. The weld bead was generally generated. The duration decided the final hairpin's appearance.

The time of the three stages together determines the minimum welding time required. Therefore, a high absorption and high power laser beam has great significance. The influence of the gap is mainly reflected in the second stage, where the surface tension drives a restoration effect. However, the recoil force caused by high power density may weaken the restoration effect.

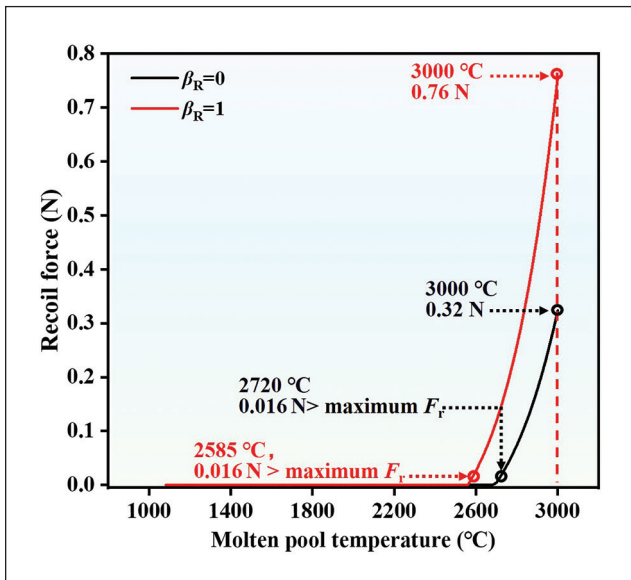


Fig. 11 – The recoil force  $F_e$  value varying with the molten pool temperature.

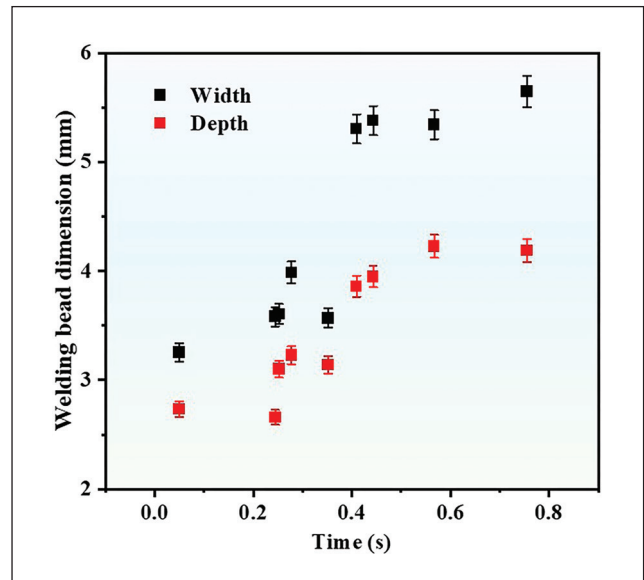


Fig. 12 – Influence of the sum time of the second and third stages on the weld bead dimensions.

## Process Parameters Optimization Strategy

There were three main process parameters when spot welding the hairpins, including the offset distance  $d$ , defocusing amount  $\Delta h$ , and welding time  $t$  with constant laser power. The offset distance decided the laser spot position; the defocusing amount determined the vertical height of the welding head; the welding time was the final processing time. The main concerns when optimizing the process parameters were weld bead appearance and the minimum time required for welding. The computational formula of the welding time  $t_{all}$  is as follows:

$$t_{all} = t_1 + t_2 + t_3 \quad (13)$$

where  $t_1$ ,  $t_2$ , and  $t_3$  are the required time for the first, second, and third stages. The relationships between the process parameters and the required times of different stages are as follows:

1. The first stage. This stage is the process before the two molten pools come into contact. It means how long it takes to form a liquid bridge between the hairpins. At this stage, the offset distance and defocusing amount are critical. Based on the results in the “Molten Pool Characteristics” section, the offset distance determines how much laser energy is radiated to the hairpin, which can be considered a direct influence. For the defocusing amount, because of copper’s high heat dissipation capacity, the high energy density caused by focusing can help form a molten pool as early as possible. Then, the two molten pools may contact each other earlier. Figure 12 presents that +3, 0 and –7 mm defocusing amounts increased the first stage time. Although the defocusing amount of 0 mm seemed to provide the most focused energy, the hairpin shortened into positive defocus after welding. Therefore, the defocusing amounts of –3 or –5 mm were better.

2. The second stage. This stage is from the two molten pools’ contact to the molten pool recovery stability and has the most

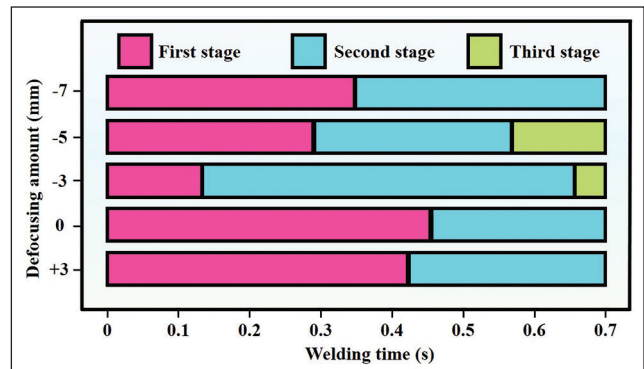


Fig. 13 – Time costs of three stages with different defocusing amounts.

complex phenomenon. There is a rapid fusion process of two molten pools at the stage, so randomness and uncertainty are strong. For the defocusing amount  $\Delta h$ , which affects the energy density, a higher energy density will lead to a more significant flow that may make the molten pool finish the second stage faster. The second stage time  $t_2$  also relates to the offset distance. If the distance is closer to the midline of the gap, the heat that transfers to the distal hairpin will be smoother. This will make it easier to pass the second stage. For the welding time  $t$ , only when  $t$  is less than the sum of the first and second stage times,  $t + t_2$  does the  $t$  need to be considered; otherwise, the second stage time is  $t - t_1$ .

3. The third stage. At this stage, the molten pool tends to be stable, and  $t$  mainly determines the time of the last stage as well as the final weld bead appearance.

The first stage mainly determines whether the weld bead can be formed and the length of the redundancy time. The second and third stages mainly relate to the appearance and dimension of the weld bead. The influence of the sum time of the second and third stages on the weld bead dimensions is

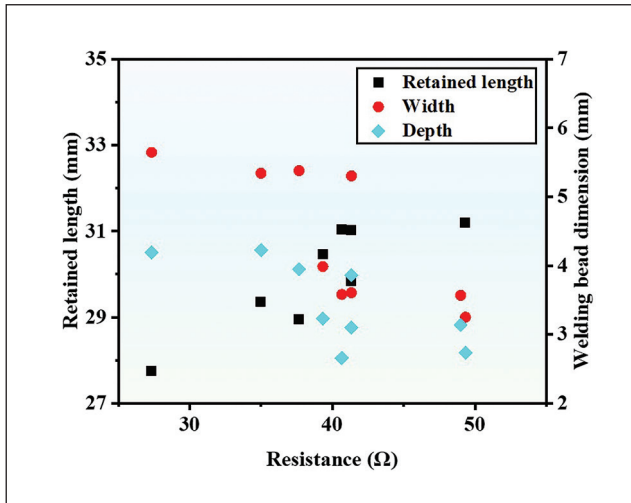


Fig. 14 – Relationships among resistance, retained length, and weld bead dimensions.

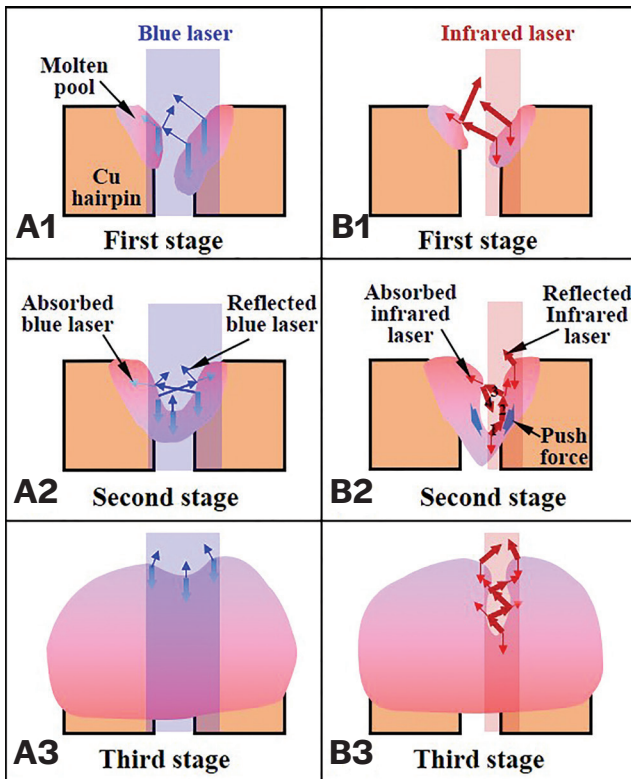


Fig. 15 – Schematic diagram of the blue and infrared laser welding of copper hairpins.

seen in Fig. 12. The longer the time, the larger the dimension. The main reason is that in the second and third stages, the molten pool can cover the laser spot and absorb the most laser energy. Laser absorb is key to affecting width and depth. It can also prove that the indeterminacy of the contact process may be an important source of unstable qualities.

For the process parameters optimization, according to the order of spot welding, the laser spot position determined by the offset distance is the first process parameter of con-

cern. When the offset distance changed from 0 to 0.6 mm, the welding effect was a gradual transition. Firstly, the two sides melted slightly and could not merge into a single molten pool. Secondly, the individual molten pool melted and merged with another micromelt pool. Finally, only a single molten pool can be formed and cannot realize welding. Therefore, the offset distance greatly influences the first stage's required time  $t_1$ , which is the most energy dissipation in spot welding. The best effect is that most of the laser spot area can radiate on the hairpin, and the liquid metal can touch each other against time.

After determining the offset distance  $d$ , the defocusing amount  $\Delta h$  is the second process parameter. For the first stage, though the defocusing amount  $\Delta h$  can also influence the violent degree of the liquid copper, which may promote the contact of the two molten pools, the influence of the violent degree is smaller than the offset distance  $d$  and is difficult to accurately control. Therefore, the defocusing amount  $\Delta h$  can be considered more at the second stage. The appearances with different defocusing amounts have been shown in Fig. 5. The time costs of the three stages with different defocusing amounts are exhibited in Fig. 13. The result showed that in the fixed time of 0.7 s, the defocusing amount affected energy absorption. When the defocusing amounts were  $-7$ ,  $0$ , and  $+3$  mm, the welding process could not go into the third stage and, especially, the first stage took too much time. The two molten pools touched each other quickly with defocusing amounts of  $-3$  or  $-5$  mm. But the  $-3$  mm defocusing amount cost more time in the second stage due to the violent flow. By contrast, the  $-5$  mm defocusing amount made the molten pool absorb the laser energy and expand more rapidly. The defocusing amount  $\Delta h$  relates to molten pool stability.

Considering the welding time  $t$ , when the offset distance and defocusing amount are constant, the influence of welding time  $t$  on appearances is shown in Fig. 5. The result showed that near-0.7 s is the minimum required time in the work. A welding time that's too long, such as 1.1 s, will enhance the instability of the molten pool because of a high temperature. Therefore, a welding time that can just finish the three stages without the molten pool slipping is best.

### Analysis of Influence Factors of Resistance

Weld bead dimension, the retained length of the copper hairpin, crystal lattice characteristics, and pore defects are key factors in the electrical resistance of pure copper. In this work, the laser power was constant at 1950 W, which is an important process parameter for crystal lattice characteristics. All the samples were spot welded similarly. There were few pores in the weld beads. Therefore, this work mainly considered the effect of weld bead dimension and retained length. The mapping relationships between the resistance and the weld bead dimensions are exhibited in Fig. 14. The results showed that larger depths and widths will lead to smaller resistance. The better-joining state results in a larger sectional size applied for current conveyance, and then resistance decreases. In addition, a large dimension will shorten the retained hairpin length. The shorter length leads to lower electrical resistance. Because the qualities of a weld bead by the blue laser are stable and guaranteed without defects, the

resistance has no abrupt change. The retained length can be predesigned. The influences of the dimensions on resistance will be weakened. Therefore, the key to welding copper hairpins with a blue laser is the choice of defocusing amount and the other process parameters for obtaining high welding efficiency.

## Comparative Analysis of Blue and Infrared Laser Welding

The results proved that a blue laser can weld copper hairpins by conduction spot welding without spatters. There were few pores in the weld bead. The required welding time was about 0.7 s. Compared with infrared laser welding with a scanning speed of 50 ~ 150 mm/s, which needs about 0.06 ~ 0.2 s welding time, as seen in Ref. 2, 0.7 s does not mean very ideal welding efficiency. However, the weld bead quality from a blue laser can be guaranteed and worth exploring. With the development of the high-power blue laser or the infrared-blue hybrid laser, shorter welding times are easy to achieve. For example, Fujio et al. (Ref. 10) have shortened the welding time of copper hairpin to 0.2 s through the infrared-blue hybrid laser.

Another important advantage of the blue laser for welding copper hairpins is the strong stability when meeting the gap. A gap will be generated due to a surplus when assembling and unavoidable assembly errors. In addition, the gap will also provide the possibility of upgrading the motor structure. First, owing to the extremely high absorption rate of the blue laser for copper, large laser spot welding with conduction mode becomes possible. The larger spot diameter provides enhanced capabilities to adapt to the larger gap and avoid the situation in Fig. 3. Second, when the molten pools contact each other at the second stage, a gap will inevitably form a depression that must be restored as soon as possible to avoid collapse. The depression has a similar effect to a keyhole, which produces multiple reflections. For the infrared laser, a large amount of laser energy will be reflected and even multi-reflected in the gap. These reflections lead to a push force from the recoil force  $F_r$ , a large value seen in Table 3. Similar results can also be found in Ref. 13. The push force will hinder restoration of the molten pool. The schematic diagram is exhibited in Fig. 15B2. For the blue laser, due to the high absorption, the most energy is absorbed by the molten pool, as shown in Fig. 15A2. Meanwhile, the blue laser can finish the second stage faster and more stably because, due to the low energy density, there is almost no metal evaporating. At last, when going into the third stage, it is a comparison between conventional conduction and keyhole welding modes. The process images of the infrared laser welding can be seen in Ref. 22. Blue laser conduction welding is more stable than infrared laser keyhole welding, as shown in Figs. 15–A3 and B3. For keyhole welding, Guo et al. (Ref. 13) presented that the keyhole led to a necking- and tip-elongated phenomenon, which formed a bubble or pore. More crucial is that when copper goes from solid to liquid to keyhole, the absorption rate of the infrared laser increases from about 3% to 15% to 60% (Ref. 4). Because the keyhole has been unstable due to the evaporation and multiple reflections, it prevents the absorption rate from being relatively constant. The rate will drastically fluctuate between about 15% and 60%. The final welding qualities are difficult to guarantee. The results from the infrared laser welding by

Dimatteo et al. (Ref. 2) also proved that it was difficult to avoid pore defects. Therefore, conduction welding can reduce this defect by avoiding the phenomenon above.

At present, there are problems with the beam-forming ability of high-power blue lasers, and it is difficult to achieve a small laser spot size. A large spot size is mainly used for conduction welding. It is also difficult to use with the galvanometer; only the laser head can be used. Therefore, this limits the further improvement of welding efficiency. If the laser spot diameter of the blue laser is the same as that of the infrared laser, owing to the high absorption, the keyhole can be more stable. The push force and potential pores resulting from the multi-reflection will be greatly weakened. The efficiency and stability of welding copper hairpins with a gap have the potential to be improved. In addition, the high cost of blue laser equipment is also one of the important issues hindering the application of the technology.

## Conclusions

The spot welding of rectangular copper hairpins was systematically studied by a 2000 W high-power blue laser for the first time. The dynamic behavior, optimization strategy, and microstructure properties were analyzed. The comparison between the blue and infrared laser for welding the copper hairpins with a gap was shown. The main conclusions are as follows:

1. With its high absorption rate for copper, a blue laser can efficiently weld two copper hairpins with a cross-sectional area of 8 mm<sup>2</sup> and a gap of 0.6 mm. There were no obvious defects and spatters. At blue laser power of 1950 W and a defocusing amount of -3 mm, the optimal welding time is 0.7 s.
2. There are three stages when spot welding copper hairpins: when the two molten pools contact, the first stage ends; in the second stage, the molten pool at the gap restores; in the third stage, the final weld bead forms. Minimizing the time required for the first stage, avoiding the molten pool of the second stage that cannot be restored, and avoiding the instability of the molten pool in the third stage are the main ideas to optimize the welding process.
3. The dynamic behavior of the molten pool at the gap was analyzed, including the shielding gas impact force  $F_s$ , recoil force  $F_r$ , gravity force  $G$ , and restore force  $F_r$ . Shielding gas impact force and recoil force both have the possibility of preventing recovery from surface tension.
4. The smallest electrical resistance can be as low as about 27 m $\Omega$ . The weld bead dimensions and the retained lengths of the copper hairpins are two important factors in influencing resistance.
5. Compared to the infrared laser relying on keyhole scanning welding, the blue laser can join the copper hairpins with conduction spot welding, which has a simpler process design.
6. This work ensures the advantage of using a high-absorption blue laser in welding copper hairpins. By optimizing the process, such as tilting the laser beam or scanning oscillation, better welding quality and efficiency may be obtained. With the development of welding technology, real-time monitoring and control based on the molten pool characteristics in the

work and the longer focal length of the welding head are the future research points.

## Acknowledgments

This work was supported by National Natural Science Foundation of China (grant numbers 52004160, 52105469, 52075327); China Postdoctoral Science Foundation (grant numbers 2021M692038, 2022T150399); and University Synergy Innovation Program of Anhui Province (grant number GXXT-2022-086).

## References

1. Tóth, T., Hensel, J., Thiemer, S., Sieber, P., and Dilger, K. 2021. Electron beam welding of rectangular copper wires applied in electrical drives. *Welding in the World* 65(11): 2077-2091. DOI: 10.1007/s40194-021-01158-4
2. Dimatteo, V., Ascari, A., Faverzani, P., Poggio, L., and Fortunato, A. 2021. The effect of process parameters on the morphology, mechanical strength and electrical resistance of CW laser-welded pure copper hairpins. *Journal of Manufacturing Processes* 62: 450–457. DOI: 10.1016/j.jmapro.2020.12.018
3. Glaessel, T., Seefried, J., and Franke, J. 2017. Challenges in the manufacturing of hairpin windings and application opportunities of infrared lasers for the contacting process. *2017 7th International Electric Drives Production Conference (EDPC)*: 1-7. DOI: 10.1109/EDPC.2017.8328150
4. Blom, A., Pique, A., Dunias, P., Sugioka, K., Herman, P. R., van Engen, P., Hoving, W., Fieret, J., Bachmann, F. G., de Kramer, J., Dubowski, J. J., Hoving, W., Washio, K., Geohegan, D. B., Traeger, F., and Murakami, K. 2003. Process spread reduction of laser microspot welding of thin copper parts using real-time control. *Photon Processing in Microelectronics and Photonics II*. DOI: 10.1117/12.478612
5. Bowman, R. L., Jack, J. R., Spisz, E. W., and Weigand, A. J. 1969. *Solar absorptances and spectral reflectances of 12 metals for temperatures ranging from 300 to 500 K*. NASA Technical Note.
6. Wang, H., Wu, Y., and Wang, H. 2021. Current status of applying the blue laser in nonferrous metals processing. *The Chinese Journal of Nonferrous Metals* 31(11): 3059-3070. DOI: 10.11817/j.ysxb.1004.0609.2021-42030
7. Tang, Z., Wei, Q., Gao, Z., Yang, H., Wang, A., Wan, L., Luo, C., Wu, Y., Wang, H., and Wang, H. 2022. 2000W blue laser directed energy deposition of AlSi7Mg: process parameters, molten pool characteristics, and appearance defects. *Virtual and Physical Prototyping* 18(1): 2120405. DOI: 10.1080/17452759.2022.2120405
8. Tang, Z., Zhang, X., Wan, L., Ouyang, Y., Gao, Z., Wei, Q., Wang, A., Yang, H., Wu, Y., Zhang, Y., Wang, H., and Wang, H. 2023. Blue laser welding of laminated electrical steels: Dynamic process, weld bead characteristics, mechanical and magnetic properties. *Journal of Materials Processing Technology* 312: 117859. DOI: 10.1016/j.jmatprotec.2023.117859
9. Tang, Z., Wan, L., Yang, H., Ren, P., Zhu, C., Wu, Y., Wang, H., and Wang, H. 2024. Stable conduction mode welding of conventional high-reflectivity metals with 2000 W blue laser. *Optics & Laser Technology* 168: 109971. DOI: 10.1016/j.optlastec.2023.109971
10. Fujio, S., Takenaka, K., Sato, Y., Ito, R., Hori, E., and Tsukamoto, M. 2022. Effect of blue diode laser intensity on welding of pure copper wire using blue-IR hybrid laser. *Journal of Laser Applications* 34(4):042021. DOI: 10.2351/7.0000795
11. Zediker, M. S., Fritz, R. D., Finuf, M. J., and Pelaprat, J. M. 2020. Laser welding components for electric vehicles with a high-power blue laser system. *Journal of Laser Applications* 32(2): 022038. DOI: 10.2351/7.0000054

12. Sun, W., Zhang, D., and Luo, M. 2021. Machining process monitoring and application: a review. *Journal of Advanced Manufacturing Science and Technology* 1(2): 2021001. DOI: 10.51393/j.jamst.2021001

13. Guo, L., Wang, H., Liu, H., Huang, Y., Wei, Q., Leung, C. L. A., Wu, Y., and Wang, H. 2023. Quantifying the effects of gap on the molten pool and porosity formation in laser butt welding. *International Journal of Heat and Mass Transfer* 209: 124143. DOI: 10.1016/j.ijheatmasstransfer.2023.124143

14. Bai, D., Gao, P., Yan, X., and Wang, Y. 2021. Intelligent forming technology: State-of-the-art review and perspectives. *Journal of Advanced Manufacturing Science and Technology* 1(3): 2021008. DOI: 10.51393/j.jamst.2021008

15. Pang, S., Hirano, K., Fabbro, R., and Jiang, T. 2015. Explanation of penetration depth variation during laser welding under variable ambient pressure. *Journal of Laser Applications* 27: 022007. DOI: 10.2351/1.4913455

16. Harrison, D., Yan, D., and Blairs, S. 1977. The surface tension of liquid copper. *The Journal of Chemical Thermodynamics* 9(12):1111-1119. DOI: 10.1016/0021-9614(77)90112-4

17. Lee, J. Y., Ko, S. H., Farson, D. F., and Yoo, C. D. 2002. Mechanism of keyhole formation and stability in stationary laser welding. *Journal of Physics D: Applied Physics* 35: 1570. DOI: 10.1088/0022-3727/35/13/320

18. Connor, N. 2020. Copper – Atomic Mass – Atomic Weight – Cu. Accessed May 7, 2023, from [periodic-table.org/Copper-atomic-mass/](http://periodic-table.org/Copper-atomic-mass/).

19. [periodic-table.org/copper-latent-heat-vaporization/](http://periodic-table.org/copper-latent-heat-vaporization/). 2023. Accessed May 7, 2023.

20. Auwal, S. T., Ramesh, S., Yusof, F., and Manladan, S. M. 2018. A review on laser beam welding of copper alloys. *The International Journal of Advanced Manufacturing Technology* 96(1-4): 475-490. DOI: 10.1007/s00170-017-1566-5

21. Nayer, A. 1997. *The Metals Databook*. New York: McGraw-Hill.

22. Hartung, J., Jahn, A., Bocksrocker, O., and Heizmann, M. 2021. Camera-based in-process quality measurement of hairpin welding. *Applied Sciences* 11(21). DOI: 10.3390/app112110375

**ZIJUE TANG, LE WAN, XIAOLIN ZHANG, CHANG-LONG ZHU, HUIHUI YANG, YI WU, and HONGZE WANG** ([hz.wang@stju.edu.cn](mailto:hz.wang@stju.edu.cn)) are with State Key Laboratory of Metal Matrix Composites, Shanghai, China, and School of Materials Science & Engineering, Shanghai Jiao Tong University, Shanghai, China. **YI WU** and **HONGZE WANG** are also with the Institute of Aluminics Materials, Shanghai Jiao Tong University (Anhui), Huaibei, China. **YUNBO HAO** and **KAI ZHAO** are with Shanghai Aerospace Equipments Manufacturer Co., Ltd., Shanghai, China. **MICHELE CHIUMENTI** is with the International Centre for Numerical Methods in Engineering, Universidad Politécnic de Cataluña, Barcelona, Spain. **HAOWEI WANG** is with Anhui Province Industrial Generic Technology Research Center for Aluminics Materials, Huaibei Normal University, Huaibei, Anhui, China.